Materials Horizons

ROYAL SOCIETY OF CHEMISTRY

COMMUNICATION

Published on 17 September 2026
Licensed under CC-BY 4.0

Check for updates

Cite this: DOI: 10.1039/d6mh01406b

Received 7th July 2026,
Accepted 16th September 2026

DOI: 10.1039/d6mh01406b

rsc.li/materials-horizons

From oxidation state redefinition to exotic 2D magnetism: a unified picture for 1T-$CrTe_2$

Bijoy Nharangatt, [a] Andrea Maslov, [b] Daniele Dragoni [b] and Federico Totti *[a]

The origin of the exciting magnetic and topological properties of the layered material 1T-$CrTe_2$ has long been obscured by an ambiguity in its formal oxidation states. By evaluating a broad range of structural, electronic, and magnetic observables available in the literature using density functional theory (DFT) and Wannier-based analysis, our integrated computational investigation shows that 1T-$CrTe_2$ is characterized by self-hole-doped Te 5p ligands, corresponding to a formal low-valent Cr^{2+}/Te^{-} electronic configuration rather than the previously assumed Cr^{3+}/Te_2^{2-} state. This unexpected Cr^{2+}/Te^{1-} finding provides an unprecedented, unified framework that rationalizes the existing experimental data. Our work further unveils a previously overlooked Cr 3d–Te 5p interaction, which places the anion's p-orbitals at the heart of the system's magnetism. A thorough understanding of the underlying nature of electronic and magnetic properties is essential for the design of spintronic devices and the discovery of new topological phases driven by correlated magnetism.

New concepts

This work demonstrates a breakthrough development in 2D magnetism by establishing a unified electronic framework for 1T-$CrTe_2$ based on a newly redefined, low-valent Cr^{2+}/Te^{1-} formal oxidation state. Unlike existing research that assumed chemically unexplainable Cr^{3+}/Te^{2-} configurations and relied on standard DFT+*U* corrections exclusively on chromium and that missed the crucial Te 5p contribution to the peculiar 1T-$CrTe_2$ magnetic properties, this study utilizes a comprehensive DFT+*U*+*V* approach that accounts for previously overlooked Cr 3d–Te 5p interactions. This methodology differentiates itself by successfully reconciling conflicting structural, spectroscopic, and magnetic experimental data overcoming the fragmented and often inconsistent interpretations of earlier theoretical studies. For materials science, this underlying concept provides critical insights into how ligand p-orbital anisotropy drives the thickness-dependent evolution of magnetic anisotropy from an in-plane easy axis in bulk to out-of-plane anisotropy in the monolayer. In a nutshell, these findings map out the deep interplay between electronic topology and charge redistribution, establishing a rigorous foundation for designing correlated 2D spintronic technologies.

1. Introduction

Intrinsic ferromagnetism in 2D materials marks a pivotal advancement toward realizing ultra-compact, energy-efficient spintronic technologies.[1–4] Among this growing family, 1T-$CrTe_2$ stands out as a layered van der Waals compound exhibiting ferromagnetism above 300 K in bulk, with in-plane magnetic anisotropy.[5–10] Remarkably, it transitions to out-of-plane magnetic anisotropy in the monolayer (ML) limit while retaining ferromagnetism around 200 K.[6] This spin reorientation highlights the intricate interplay between reduced dimensionality, spin–orbit coupling (SOC), and electron correlation, making ML 1T-$CrTe_2$ a promising platform for spintronic and valleytronic applications.[11]

Recent studies have substantially expanded the understanding of the structural, magnetic, transport and device-relevant properties of 1T-$CrTe_2$. From a many-body perspective, DFT+DMFT calculations have indicated a self-doped double-exchange picture with pronounced Hund metallicity, characterized by the coexistence of itinerant e_g electrons and localized t_{2g} moments. This description gives rise to an effective mixed-valence-like electronic character.[13] Beyond this many-body perspective, theoretical studies have also examined the strain and electric field dependence of magnetization in ML and bilayer $CrTe_2$.[14] Experimental investigations have further addressed thickness and crystalline-dependent magnetic and transport properties,[15] interfacial enhancement of T_c in $CrTe_2$-based heterostructures,[16] and interlayer charge transfer driven multiferroicity.[17]

Despite these advances, the electronic configuration and charge distribution in 1T-$CrTe_2$ remain subject to different interpretations. In particular, Cr^{4+} has been inferred from the measured magnetic moment,[5] whereas Cr^{3+} has been suggested

[a] *Dipartimento di Chimica "Ugo Schiff" & INSTM RU, Università degli Studi di Firenze, Via della Lastruccia 3, 50019 Sesto Fiorentino (FI), Italy. E-mail: federico.totti@unifi.it*

[b] *Leonardo S.p.A., Piazza Monte Grappa, 4, 00195 Roma (RM), Italy*

by electronic-structure studies,[12] raising questions regarding charge neutrality and the extent and nature of Cr–Te hybridization.

These discrepancies motivate a microscopic examination of the orbital and bonding character of the Cr–Te electronic structure. In this work, we employ a DFT+*U*+*V* framework to provide an orbital and bonding-resolved description of the system. We investigate the Cr d orbital population, Te 5p-derived states, Cr–Te hybridization, and Te spin polarization, and relate these features to the structural, magnetic, and electronic properties observed experimentally in the literature. Our analysis further identifies an active role of Te 5p states in the ferromagnetic interactions, providing a complementary ligand-centred perspective on the microscopic magnetic mechanism of 1T-$CrTe_2$.

Standard DFT+*U* with a Hubbard correction only on Cr 3d states provides an improved description of the localization of the metal 3d electrons but does not explicitly account for the intersite interactions associated with the Cr–Te covalency. DFT+*U*+*V* extends the description of localized electrons by incorporating the intersite interactions, thereby providing a more accurate treatment of covalent interactions and electron hybridization.[18–20] In ligand-mediated exchange systems, incorporating Coulomb interactions on ligand p orbitals is important for capturing the balance between covalent and ionic interactions, which in turn influence their magnetic and spectroscopic properties.[21–24] Indeed, the coordination bond allows spin delocalization (usually a small fraction) from the metal to the ligands due to retaining a non-negligible covalent nature. Accordingly, we show that including Coulomb interactions on both Cr 3d and Te 5p states within DFT+*U*+*V* yields a consistent description of both bulk and ML 1T-$CrTe_2$ beyond what is achieved by standard DFT+*U*. Furthermore, it offers a physically motivated rationale for the underlying Cr–Te interactions and proposes a new formal oxidation state description, Cr^{2+}/Te^{-}.

Accordingly, our framework also uncovers how magnetic anisotropy evolves from in-plane in bulk $CrTe_2$ to out-of-plane in the ML. Together, these results demonstrate that correlations on both transition-metal and ligand sites are essential for understanding magnetism and topology in 1T-$CrTe_2$, establishing a foundation for designing correlated 2D magnets.

2. Computational methods

All calculations were performed using density functional theory (DFT) as implemented in the Quantum ESPRESSO package.[25,26] The Perdew–Burke–Ernzerhof (PBE) exchange–correlation functional within the generalized gradient approximation (GGA) was employed.[27] The inclusion of van der Waals interactions is essential for obtaining a reliable interlayer distance in 1T-$CrTe_2$. To account for long-range dispersion interactions, typically underestimated by GGA, the DFT-D3 correction scheme proposed by Grimme was applied.[28]

A plane-wave basis set with a kinetic energy cutoff of 80 Ry for the wavefunctions and 800 Ry for the charge density was adopted. Brillouin zone integrations were performed using Monkhorst–Pack *k*-point meshes of 12 × 12 × 8 for bulk and 14 × 14 × 1 for monolayer calculations. A vacuum spacing of more than 15 Å was introduced along the out-of-plane direction in monolayer calculations to eliminate interlayer interactions.

All atomic structures were relaxed using the Broyden–Fletcher–Goldfarb–Shanno (BFGS) algorithm[29] until the total energy difference between consecutive steps was less than 10^{-6} Ry and the atomic forces were below 10^{-3} Ry $Bohr^{-1}$. Cold smearing as proposed by Marzari and Vanderbilt[30] was used, with a smearing width of 0.002 Ry to ensure numerical stability. We used the DFT+*U*+*V* method as formulated by Dudarev and implemented in Quantum ESPRESSO.[31,32] To characterize the Cr–Te bonding and electrostatic interactions further, we performed additional analyses using the LOBSTER code.[33] The integrated crystal orbital bond index (ICOBI) was calculated to quantify the strength of the Cr–Te bonds, while the Gross population analysis was used to evaluate the electron populations. In addition, Madelung energy was evaluated to assess the electrostatic contribution to the bonding. Additional calculation details are provided in section S1 of the SI.

3. Results and discussion

3.1. Crystal structure

The 1T phase of bulk $CrTe_2$ synthesized *via* oxidative deintercalation of $KCrTe_2$ has lattice parameters $a = b = 3.7887$ Å and $c = 6.0955$ Å (trigonal space group $P\bar{3}m1$) (Fig. 1).[5] However, this phase is metastable and decomposes above 330 K. Zhang *et al.* demonstrated the successful synthesis of high-quality stoichiometric 1T-$CrTe_2$ thin films, from the ML limit up to seven

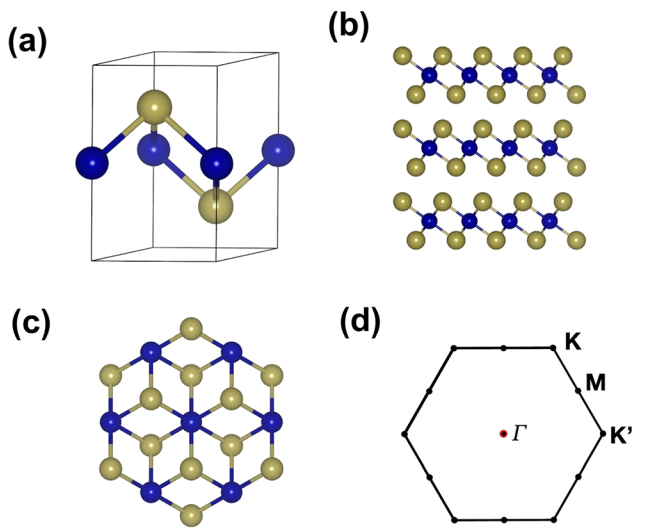

Fig. 1 (a) Trigonal lattice of 1T-$CrTe_2$ with one Cr atom (blue) and two Te atoms (brown) per unit cell. (b) Side view of the layered structure showing van der Waals coupling between different 1T-$CrTe_2$ units along the *c*-axis. (c) Top view illustrating the octahedral coordination of Cr by Te atoms within a single layer. (d) First Brillouin zone of the hexagonal lattice, showing high-symmetry points Γ, M, K, and K′ relevant to the electronic structure analysis in later figures.

This journal is © The Royal Society of Chemistry 2026

layers, grown on graphene/SiC. Their work unambiguously established robust ferromagnetism in the ML with a Curie temperature of $\sim$200 K.[6] In contrast, a recent study reported a temperature-dependent growth behavior and claimed an antiferromagnetic ML.[48] However, that study grows the films at substrate temperatures $\geq$600-900 °K, a regime where bulk $CrTe_2$ is known to be metastable and begins transforming into Cr-intercalated phases (*e.g.*, Cr_2Te_3, Cr_5Te_8) above $\sim$500–650 K.[9] Therefore, in the present work, we focus on the 1T-$CrTe_2$ phase realized by Zhang *et al.*[6]

Early experiments suggested Cr^{4+}/Te^{2-} oxidation states[5] in bulk 1T-$CrTe_2$. Although our PBE calculations yield bulk lattice parameters ($a = b$ = 3.75 Å, c = 5.96 Å) in good agreement with experiments ($a = b$ = 3.81 Å, c = 6.10 Å), the ML lattice parameters ($a = b$ = 3.62 Å) deviate substantially from the experimental value ($a = b$ = 3.91 Å).[17] Moreover, the hole pockets near the Fermi energy reported in the experimental angle-resolved photoemission spectroscopy (ARPES)[6] for 1T-$CrTe_2$ (Fig. S2) are absent from the PBE band structure (Fig. S1). The calculated Cr 3d population and magnetic moments ($2.5\mu_B$ on Cr and $-0.1\mu_B$ on Te) suggest more a Cr^{3+} ($3d^3$) than a Cr^{4+} ($3d^2$), and the Te as essentially diamagnetic Te (Te^{2-}) with a consequent clear mismatch in the charge balance. Similar results were obtained in the previous DFT+U calculations, where U was applied only to Cr[12] (Table S1 and Fig. S1), as well as in DFT+DMFT calculations.[13] These results highlight the limitations of standard PBE/PBE+U_{Cr} in capturing the strong correlations and charge transfer in 1T-$CrTe_2$. On the other hand, XAS spectra of CrTe[34] and $Zn_{1-x}Cr_xTe$,[35] where the presence of Cr^{2+} is proposed, closely match those obtained in ref. 6 for 1T-$CrTe_2$ (in all three cases, the Cr L3 and L2 edges occur at approximately 574 eV and 584 eV, respectively).

To further elucidate the electronic structure, we employed the PBE0 hybrid functional as an independent higher-level approximation. Hybrid functionals are known to provide an improved description of localized 3d states in many transition-metal systems,[20,26,36,37] although their applicability to metallic and strongly hybridized materials remains system dependent. In the present case, PBE0 yields enhanced magnetic moments ($\sim 3.6\mu_B$ on Cr and $-0.5\mu_B$ on Te) and a more localized Cr-3d character (Fig. S2) shifted away from the Fermi level. The electronic states near E_F are instead predominantly Te 5p-derived, in agreement with the experimental ARPES spectra, providing a complementary perspective on the degree of electronic localization.

To obtain a computationally tractable yet physically motivated description, we adopted a DFT+U+V framework including both on-site (U) and intersite ($V_{Cr–Te}$) interactions. The corresponding parameters were determined by considering the agreement with experimental structural, magnetic, and spectroscopic data, while the resulting electronic structure was further compared with the higher-level PBE0 hybrid calculations (Fig. S3). Thus, PBE0 serves as an independent theoretical reference rather than as a definitive benchmark for the DFT+U+V description.

Linear-response theory, as implemented in the HP code,[38] yields finite U and V values for both Cr and Te, thereby defining the physically relevant parameter regime. While these values do not quantitatively reproduce the experimental lattice parameters (Table S1), they provide a grounded starting point for further refinement. Within this range, moderate adjustments of the interaction parameters were made to achieve a simultaneous and internally consistent description of the different physical manifolds, including structural (Table 1), magnetic (Table 3), and electronic properties, for both bulk and monolayer 1T-$CrTe_2$.

Table 1 The calculated lattice parameters and geometrical parameters of 1T-$CrTe_2$ for the bulk and the ML

	$a = b$ (Å)	c (Å)	Cr–Te (Å)	Te–Cr–Te (°)
Bulk	3.87 (ref. 6)	6.10 (ref. 6)	2.75	90.8
ML	3.91 (ref. 17)	20.0	2.76	89.7

The resulting parameter set (U_{Cr} = 5 eV, U_{Te} = 4 eV, $V_{Cr–Te}$ = 1.0 eV) should therefore be viewed as a physically reasonable choice within this framework, enabling a unified description across multiple observables for both bulk and ML.

To assess the robustness of the calculated properties with respect to the choice of Hubbard parameters, we performed additional calculations by varying the on-site Coulomb interactions and intersite interaction around the optimized values of U_{Cr} = 5 eV, U_{Te} = 4 eV, and $V_{Cr–Te}$ = 1 eV. Specifically, U_{Cr}, U_{Te}, and $V_{Cr–Te}$ were varied within the ranges of 4–6 eV, 3–5 eV, and 0.5–1.5 eV, respectively. The calculated in-plane lattice parameter $a = b$ varies only slightly, from 3.84 to 3.89 Å, while the Cr d-electron occupation remains close to 4 e^- (3.8–4.14). Importantly, the magnetic moments are also relatively insensitive to these parameter variations, with the Cr and Te moments remaining close to $4\mu_B$ and $-1\mu_B$, respectively. These results indicate that the structural and magnetic characteristics discussed in this work are robust against reasonable variations of the Hubbard parameters and are therefore not a consequence of a particular finely tuned choice of U and V. The complete set of calculations is provided in Table S2.

To assess the physical role of the Coulomb interactions, we further examined the Cr–Te bonding using ICOBI and Madelung energies (Table 2). All calculations in this comparison were performed on the same optimized crystal structure, with only the Coulomb parameters varied, allowing the electronic and bonding effects of U_{Cr}, U_{Te}, and $V_{Cr–Te}$ to be isolated from structural relaxation effects. In PBE, the relatively large ICOBI values indicate a moderate covalent contribution, whereas the less negative Madelung energy points to weaker electrostatic stabilization. Introducing U_{Cr} reduces the ICOBI, accompanied by a substantial increase in the electrostatic stabilization.

Table 2 Role of Coulomb interactions in Cr–Te bonding

U_{Cr} (eV)	U_{Te} (eV)	$V_{Cr–Te}$ (eV)	Madelung energy (eV)	ICOBI spin up	ICOBI spin down
5	4	1	−2.07	0.36	0.34
5	4	0	−1.96	0.32	0.30
5	0	0	−1.36	0.35	0.34
0	0	0	−0.95	0.48	0.49

Including U_{Te} further strengthens the Madelung contribution, while only slightly reducing the ICOBI, indicating that the ligand correction primarily enhances the ionic character without strongly suppressing the Cr–Te covalent interaction. Finally, the inclusion of the intersite V_{Cr-Te} further slightly enhances both the electrostatic stabilization and the Cr–Te bond index. These results show that the inclusion of ligand and intersite Coulomb interactions is important for capturing the non-trivial balance between ionic and covalent contributions to the Cr–Te bonding that underlies the ligand-mediated magnetic coupling.

3.2. Magnetism

We analyzed the magnetic interactions by calculating exchange coupling constants J_{ij} using the Green's function method, based on the Heisenberg Hamiltonian.

$$E = -\sum_{i,j} J_{ij} S_i \cdot S_j \quad (1)$$

In bulk 1T-$CrTe_2$, both intra-layer (J_1) and inter-layer (J_2) exchange interactions exist, while only intra-layer (J_1) interactions are present in the ML. The calculated exchange constants for both bulk and ML structures (Table 3) consistently support a ferromagnetic ground state, in agreement with experimental reports.[5–9]

To complete the magnetic characterization, we calculated the magnetocrystalline anisotropy energy (MAE) as the energy difference between spin alignment along the in-plane (100) and out-of-plane (001) directions:

$$\mathrm{MAE} = E(100) - E(001) \quad (2)$$

where $E(100)$ and $E(001)$ represent the total energies for spin alignments along the (100) and (001) crystallographic directions, respectively.

As reported in experiments, bulk $CrTe_2$ favors in-plane magnetic anisotropy, while the ML exhibits a smaller out-of-plane anisotropy. The Curie temperature was computed using classical Monte Carlo simulations, including the exchange interactions and anisotropy energies. The resulting Curie temperatures for both bulk and monolayer (Table 2) are consistent with the range of experimentally reported values, indicating that the DFT+U+V framework captures the main trends of the magnetic interactions.

3.3. Electronic structure

To further assess the proposed chemical picture, we compare the calculated electronic structure with the available ARPES data for 1T-$CrTe_2$ at different layer thicknesses. For a nominal thickness of 7 ML, experimental spectra along the M–Γ–K direction[6] are compared with results obtained from our Wannier-based tight-binding model (Fig. 2 and Fig. S4).

The ARPES measurements shown in Fig. 2 were obtained at $h\nu$ = 21.2 eV. At this photon energy, the photoelectron mean free path is limited to ∼0.5–1 nm, and the spectral weight of minority-spin states is significantly affected by matrix-element effects, as reported experimentally.[6] In addition, finite thickness can introduce quantization effects that are not explicitly captured in bulk-derived models. The experimental films are also supported by a substrate, which may introduce additional effects such as charge transfer, interfacial hybridization, strain, screening, and inversion-symmetry breaking. However, the interaction between 1T-$CrTe_2$ and bilayer graphene is predominantly weak and van der Waals in nature. Therefore, the substrate effects are expected to be relatively small compared with the intrinsic properties of the $CrTe_2$ layer.

Our Wannier-based calculations are based on a bulk tight-binding Hamiltonian and therefore do not include substrate effects, matrix-element-dependent intensity variations or thin-film quantization. As a result, direct comparison of band dispersions, linewidths, or spectral intensities is expected to be semi-quantitative. The comparison is therefore restricted to robust features of the electronic structure, such as the presence and momentum-space location of electron and hole pockets.

The asymmetric PDOS shows spin polarization of Cr and Te (Fig. 3). The occupied majority-spin (up) channel is dominated by localized Cr 3d states, while the minority-spin (down) channel is mainly composed of Te 5p and crosses E_F. Up-spin Te states dominate near E_F, giving metallic behavior for spin-up and nearly insulating behavior for spin-down, confirming the spin-polarized half-metallic nature of 1T-$CrTe_2$. This electronic picture is different from the one computed at the PBE level (Fig. S3), where both Cr and Te states are contributing at E_F.

In 1T-$CrTe_2$, Cr is octahedrally coordinated by Te, leading to the conventional t_{2g}–e_g crystal field splitting. The spin-dependent hybridization between Cr 3d and Te 5p states further modifies this level scheme, lifting the t_{2g} degeneracy into a lower-energy d_{xy} manifold and a degenerate d_{xz}/d_{yz} manifold (π interactions). The moderate covalent component of the Cr–Te interaction is supported by the Cr–Te ICOBI values of 0.36 and 0.34 for the up-spin and down-spin channels, respectively, as obtained from LOBSTER. The resulting orbital level splitting is reflected in the corresponding orbital populations, which yield an approximately d^4 Cr configuration. This orbital redistribution is accompanied by a substantial change in the electrostatic environment upon inclusion of intersite V_{Cr-Te}, as reflected by the Madelung contribution, which changes from −0.5 eV (calculated using the PBE relaxed

Table 3 Computed magnetic exchange interaction, magnetic anisotropic energy, and Curie temperature (experimental values in parentheses)

	J_1 (cm^{-1}) (intralayer)	J_2 (cm^{-1}) (interlayer)	MAE (cm^{-1})	T_c (K)
Bulk	32.6 [4.0 meV]	5.6 [0.69 meV]	−45.05 [−5.6 meV]	325 (∼310) (ref. 6)
ML	32.4 [4.0 meV]		11.68 [1.4 meV]	225 (∼200) (ref. 6)

This journal is © The Royal Society of Chemistry 2026

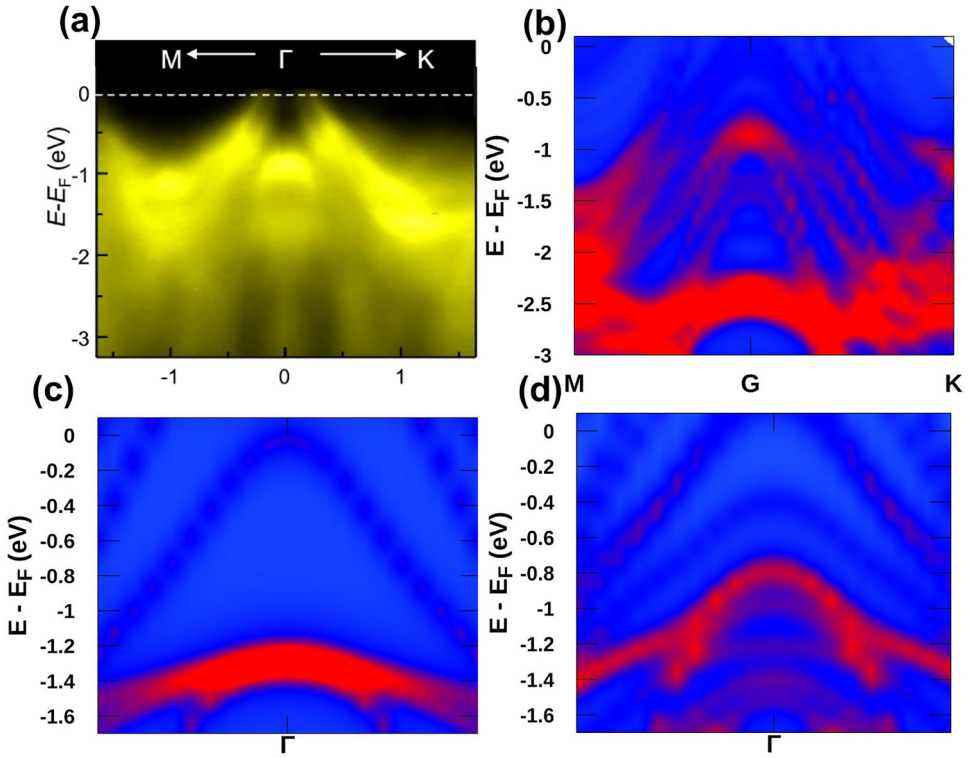

Fig. 2 (a) Experimental angle-resolved photoemission spectroscopy (ARPES) spectrum for a 7-layer 1T-$CrTe_2$ film (reproduced from ref. 6; available under a CC-BY 4.0 license. Copyright Springer, Zhang *et al.*) taken along the M–Γ–K path. (b) Simulated surface spectral function for a 7-layer slab of 1T-$CrTe_2$, calculated using WannierTools. The computed ARPES spectra reproduce key experimental features, including hole-like valence bands near the Fermi energy (E_F) at Γ and electron pockets at the M point (see Fig. S4). (c) and (d) ARPES simulations for ML and bilayer 1T-$CrTe_2$, respectively, are plotted along M–Γ–M, showing the evolution of the band structure with increasing thickness (see SI, Fig. S5 for the comparison of the bands for ML and bilayer with the experimental ARPES). The Fermi level is set to 0 eV in all panels. The calculation includes SOC and was performed using a tight-binding model derived from bulk Wannier90 data.

structure) in PBE to −2.07 eV in DFT+*U*+*V*. In contrast, ICOBI remains close to the value reported in Table 2 for PBE, irrespective of whether it is evaluated using the PBE-relaxed or DFT+*U*+*V*-relaxed structure. This indicates a substantial modification of the electrostatic environment associated with charge redistribution.

The PDOS and band structure further reveal that the low-energy unoccupied spectral weight is predominantly Te 5p-derived rather than being confined to the Cr 3d manifold, while the more localized Cr 3d states are shifted away from E_F. This redistribution of spectral weight, arising from spin dependent Cr 3d–Te 5p hybridization in stoichiometric $CrTe_2$, gives rise to intrinsic Te 5p ligand hole character within the charge-neutral lattice rather than extrinsic hole doping. The Te 5p-derived states near E_F therefore play an active role in the half-metallic electronic structure and magnetic response of 1T-$CrTe_2$. The near zero Te–Te ICOBI values (0.03 and 0.01 for the up-spin and down-spin channels respectively) further indicate that this ligand-mediated behaviour is not associated with significant Te–Te dimerization but rather with the Cr–Te hybridization.

Also, the integration of the occupied Cr-3d/Te-5p PDOS yields four and one unpaired electrons on Cr and Te, respectively. The corresponding magnetic moments are $4\mu_B$ on Cr and $-1\mu_B$ on each Te, resulting in a net magnetic moment of $2\mu_B$ per formula unit. The population analysis, which indicates a d^4 configuration for Cr, together with these results, suggests that the system is best described by a formal Cr^{2+}/Te^{-} electronic configuration. In this context, oxidation states are used as an effective, chemically motivated descriptor to rationalize bonding and magnetism, rather than as uniquely defined charges. The combined evidence from stoichiometry, orbital character, and spin population supports a chemically meaningful assignment of the Cr oxidation state relative to the Te sublattice and highlights the limitations of the commonly assumed Cr^{3+} description often adopted in the literature. From a chemical perspective, this behavior is naturally explained by the π-acceptor nature of Te, which stabilizes low effective oxidation states of the transition metal.

The three up-spin bands crossing E_F have the nature of anti-bonding p_x/p_y and p_z, and there are no metal states at E_F. So, we cannot claim that we are either in the presence of usual itinerant magnetism or a purely localized superexchange interaction. Here, the ferromagnetic ground state stabilization comes through kinetic-energy gain associated with the π-acceptor mechanism whereby ligand-derived itinerant carriers lower their kinetic energy in a ferromagnetically aligned background of localized Cr moments. This coupling is enabled by

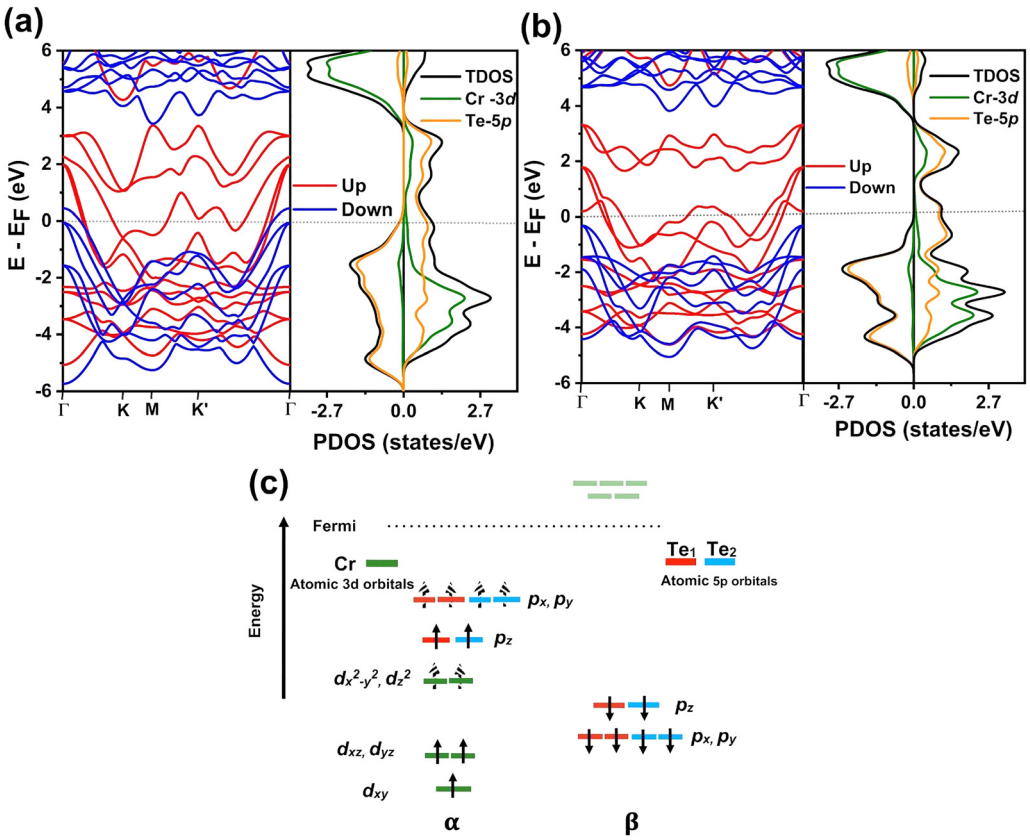

Fig. 3 (a) Spin-polarized electronic band structure and projected density of states (PDOS) for bulk 1T-$CrTe_2$, showing contributions from Cr 3d (green) and Te 5p orbitals (orange). The majority (α) and minority (β) spin channels are shown separately. (b) Same as (a), but for an ML. (c) Broken-symmetry orbital-level scheme derived from Wannier-based projection, showing the occupations of Cr and Te orbitals. Arrows indicate the spin orientation of the occupied state, with black and white alternating arrows representing half-filled states. Cr levels are shown in green, and the two inequivalent Te atoms are distinguished using red and blue colors.

hybridization between the Te 5p states and spin polarized Cr 3d orbitals, which induces spin polarization on the otherwise weakly magnetic Te states. Intra-atomic Hund's coupling on Cr then couples the itinerant ligand states to the localized Cr moments, enabling the ligand-mediated kinetic energy gain that stabilizes the ferromagnetic state.[39,40] The same mechanism also mediates interlayer spin interactions: the spatially extended Te p_z orbitals provide an efficient hopping channel across layers, enhancing the interlayer exchange J_2 to a sizable fraction of the intralayer J_1, consistent with the ligand-mediated nature of magnetism in this system.

This electronic structure differs from the self-doped double-exchange picture proposed in ref. 13, where DFT+DMFT yields a dual character of the Cr 3d states, with relatively localized t_{2g} moments coexisting with more itinerant e_g states that retain appreciable Cr-3d spectral weight at E_F, together with only weak spin polarization of the Te 5p states. In our calculations, in contrast, the itinerant states at E_F are predominantly Te-5p derived. Therefore, although both pictures involve a kinetic-energy gain upon ferromagnetic alignment, the microscopic origin of the itinerant carriers is conceptually different. In our case, the kinetic-energy gain is mediated by ligand-derived Te-5p carriers whose spin polarization and coupling to the localized Cr moments arise from Cr–Te p–d hybridization. We therefore refer to this mechanism as ligand-mediated kinetic-energy-driven ferromagnetism rather than conventional or self-doped metal-d double exchange.

Our computational framework can also provide a key insight into the underlying mechanism driving the evolution of MAE, rationalizing the transition from an in-plane easy axis in bulk 1T-$CrTe_2$ to out-of-plane anisotropy in its ML form. This is a very important aspect that has raised particular interest in the literature for its potential application in spintronic devices and magnetic memory technologies.[41–43] Nevertheless, its microscopic origin has remained elusive. Through a localized orbital-based investigation of SOC effects and PDOS, we were able to identify the ligand (Te) p-orbital anisotropy as a key driver of this transition.

Indeed, by calculating orbital-resolved fractional occupations near E_F, we observed that the out-of-plane Te p_z orbitals (aligned along the magnetization direction in ML) exhibit an enhanced exchange splitting and increased partial occupation in the ML compared to bulk (Tables S3 and S4). We confirmed that Te p_z orbitals dominate the band structures around the E_F in the ML, while in bulk, the occupations of p_x/p_y and p_z remain nearly isotropic in the same range of energies. The exchange splitting of p_z orbitals increases, while that of p_x/p_y decreases, passing from bulk to ML.

 This journal is © The Royal Society of Chemistry 2026

This anisotropic onset of Te p orbitals can therefore be ascribed to the removal of interlayer coupling and the altered screening in the ML, which strengthens SOC-induced hybridization along the out-of-plane direction. This is in agreement with the observed decrease in energy of the Te-based band near E_F, passing from 1 ML to 2 MLs (Fig. S6). As a consequence, the system lowers its energy when the magnetization aligns out-of-plane, favoring perpendicular magnetic anisotropy (PMA) in the ML. In contrast, in the bulk, stronger interlayer coupling and more efficient screening suppress p_z orbital dominance, resulting in an in-plane magnetic easy axis. In a nutshell, the enhanced p_z orbital character in the monolayer increases the spin–orbit coupling along the out-of-plane direction, favoring perpendicular magnetic anisotropy, whereas bulk interlayer coupling suppresses this effect.

A final comment on the newly proposed interpretation of the experimental data is due. The magnetic data reported in the literature exhibit several inconsistencies, which can largely be attributed to both the intrinsic complexity of the measurements and the interpretative bias introduced by computational results cited in their support.[5–7] In both cases, a key oversight lies in the neglect of the strongly spin-polarized nature of the Te ions, a factor critical for accurately reproducing experimental XAS and XMCD spectra, as well as for performing reliable *ab initio* calculations.[6] Indeed, in publications where these measurements are reported for 1T-$CrTe_2$(6), as well as in studies of related compounds, signatures of a paramagnetic contribution from Te are evident.[20,21] Omitting this contribution in spectral simulations may result in a misrepresentation of the magnetic ground state. Accurate modeling thus requires careful inclusion of the number of d holes, spin correction factors, and the averaged magnetic dipole term.[44–46]

4. Conclusion

Taken together, the chemical insights and computational strategy developed in this work lead to a coherent interpretation of experimental observations that were previously inconsistent. The new interpretation has been achieved through the systematic modelling of structural, electronic, and magnetic properties. The refined electronic framework offers a deeper understanding of layered magnetic systems and supports a physically grounded reinterpretation of experimental trends in related materials. This study also highlights the importance of the information conveyed by the formal definition of chemical oxidation states and uses them as a driver to implement a rigorously optimized computational methodology to faithfully reproduce the bonding nature of such complex 2D systems. Such a rigorously validated approach is essential for the rational design of future 2D nanoscale magnetic technologies, where complex, but intriguing, electronic structures are present.

Author contributions

B. N.: investigation, formal analysis, writing – original draft, and writing – review and editing. A. M.: fund acquisition, and writing – review and editing. D. D.: fund acquisition and writing – review and editing. F. T.: conceptualization, supervision, fund acquisition, formal analysis, and writing – review and editing.

Conflicts of interest

The authors declare that they have no conflicts of interest.

Data availability

All data supporting the findings of this study are available in the paper and/or the supplementary information (SI). Supplementary information: computational methods; PDOS plot with functionals PBE, PBE0 and PBE+*U*+*V*; ARPES spectra for different thicknesses and the Fermi surface plot, the structural data for bulk and ML. See DOI: https://doi.org/10.1039/d6mh01406b.

Acknowledgements

This work was supported by the European Union through the Next Generation EU funds through the Italian MUR National Recovery and Resilience Plan, Mission 4 Component 2 – Investment 1.4 – National Center for HPC, Big Data, and Quantum Computing (CUP B83C22002830001, Innovation Grant ASGARD). We also acknowledge the support of MUR through Progetto Dipartimenti di Eccellenza 2023–2027 (CUP B97G22000740001 – DICUS 2.0). The computing resources and the related technical support used for this work have been provided by both the National Center for HPC, Big Data, and Quantum Computing (CUP B83C22002830001, Innovation Grant ASGARD) and the CRESCO/ENEAGRID High Performance Computing infrastructure and its staff[47] that is funded by ENEA, the Italian National Agency for New Technologies, Energy and Sustainable Economic Development, and by Italian and European research programmes; see https://www.cresco.enea.it/english for information.

References

1 C. Gong, *et al.*, Discovery of intrinsic ferromagnetism in two-dimensional van der Waals crystals, *Nature*, 2017, **546**, 265–269, DOI: 10.1038/nature22060.
2 B. Huang, *et al.*, Layer-dependent ferromagnetism in a van der Waals crystal down to the monolayer limit, *Nature*, 2017, **546**, 270–273, DOI: 10.1038/nature22391.
3 Y. Deng, *et al.*, Gate-tunable room-temperature ferromagnetism in two-dimensional Fe_3GeTe_2, *Nature*, 2018, **563**, 94–99, DOI: 10.1038/s41586-018-0626-9.
4 Z. Fei, *et al.*, Two-dimensional itinerant ferromagnetism in atomically thin Fe_3GeTe_2, *Nat. Mater.*, 2018, **17**, 778–782, DOI: 10.1038/s41563-018-0149-7.
5 D. C. Freitas, *et al.*, Ferromagnetism in layered metastable 1T-$CrTe_2$, *J. Phys.: Condens. Matter*, 2015, **27**, 176002, DOI: 10.1088/0953-8984/27/17/176002.

6 X. Zhang, *et al.*, Room-temperature intrinsic ferromagnetism in epitaxial $CrTe_2$ ultrathin films, *Nat. Commun.*, 2017, **12**, 2492, DOI: 10.1038/s41467-021-22777-x.

7 A. Purbawati, *et al.*, Stability of the in-plane room temperature van der Waals ferromagnet Chromium Ditelluride and its conversion to chromium-interleaved $CrTe_2$ compounds, *ACS Appl. Electron. Mater.*, 2023, **5**, 764–774, DOI: 10.1021/acsaelm.2c01256.

8 X. Sun, *et al.*, Room temperature ferromagnetism in ultrathin van der Waals crystals of 1T-$CrTe_2$, *Nano Res.*, 2020, **13**, 3358–3363, DOI: 10.1007/s12274-020-3021-4.

9 X. Zhang, *et al.*, Substantially enhanced spin polarization in epitaxial $CrTe_2$ quantum films, *Adv. Mater.*, 2025, **37**, e2411137, DOI: 10.1002/adma.202411137.

10 A. Purbawati, *et al.*, Correction to: In-plane magnetic domains and Néel-like domain walls in thin flakes of the room temperature $CrTe_2$ van der Waals ferromagnet, *ACS Appl. Mater. Interfaces*, 2021, **13**, 59592, DOI: 10.1021/acsami.1c22588.

11 D. Xiao, G.-B. Liu, W. Feng, X. Xu and W. Yao, Coupled spin and valley physics in monolayers of MoS_2 and other group-VI dichalcogenides, *Phys. Rev. Lett.*, 2012, **108**, 196802, DOI: 10.1103/PhysRevLett.108.196802.

12 S. Li, S. Wang, B. Tai, W. Wu, B. Xiang, X. Sheng and S. A. Yang, Tunable anomalous Hall transport in bulk and two-dimensional 1T-$CrTe_2$: A first-principles study, *Phys. Rev. B*, 2021, **103**, 045114.

13 D. H. D. Lee, H. J. Lee, T. J. Kim, M. Y. Jeong and M. J. Han, Many-body electronic structure, self-doped double-exchange, and Hund metallicity in 1T-$CrTe_2$ bulk and monolayer, *npj 2D Mater. Appl.*, 2026, **10**, 41699, DOI: 10.1038/s41699-026-00670-9.

14 F. Li, B. L. Chittari, C. Lei and J. Jung, Near room temperature magnetoelectric response and tunable magnetic anisotropy in the two-dimensional magnet 1T-$CrTe_2$, *Phys. Rev. B*, 2026, **113**, 094440, DOI: 10.1103/5cmn-tgfx.

15 N. Kumar, *et al.*, Growth and investigations of the two-dimensional van der Waals $CrTe_2$ films by the sputtering route: Influence of crystallinity and film thickness on magnetization and transport behavior, *Phys. Rev. Appl.*, 2025, **25**, 014034, DOI: 10.1103/xrkt-ft57.

16 Z. Fu, *et al.*, Enhancing Curie temperature for $CrTe_2$-containing heterostructures *via* interfacial engineering, *Nano Lett.*, 2026, **26**, 3865–3872, DOI: 10.1021/acs.nanolett.6c00077.

17 D. Tian, *et al.*, Room-temperature two-dimensional multiferroic metal with voltage-controllable magnetic order, *Nat. Mater.*, 2026, **25**, 956–963, DOI: 10.1038/s41563-026-02537-2.

18 R. Mahajan, *et al.*, Importance of intersite Hubbard interactions in β-MnO_2: A first-principles DFT+U + V study, *Phys. Rev. Mater.*, 2021, **5**, 104402, DOI: 10.1103/PhysRevMaterials.5.104402.

19 N. Naveas, *et al.*, First-principles calculations of magnetite (Fe_3O_4) above the Verwey temperature using self-consistent DFT+U + V, *J. Chem. Theory Comput.*, 2023, **19**, 8610–8623, DOI: 10.1021/acs.jctc.3c00860.

20 D. M. Korotin *et al.*, Parameterizing DFT+U + V from hybrid functionals: A Wannier-function-based approach for strongly correlated materials, *arXiv*, 2026, , DOI: 10.48550/arXiv.2602.20814.

21 J. A. Chan, S. Lany and A. Zunger, Electronic correlation in anion p orbitals impedes ferromagnetism due to cation vacancies in Zn chalcogenides, *Phys. Rev. Lett.*, 2009, **103**, 016404, DOI: 10.1103/PhysRevLett.103.016404.

22 S. Ninova, *et al.*, Valence electronic structure of sublimated Fe_4 single-molecule magnets: an experimental and theoretical characterization, *J. Mater. Chem. C*, 2014, **2**, 9599–9608, DOI: 10.1039/C4TC01647E.

23 S. K. Pandey, *et al.*, Microscopic origin of room-temperature ferromagnetism in Sr_2FeReO_6, *Phys. Rev. B*, 2022, **105**, 214422, DOI: 10.1103/PhysRevB.105.214422.

24 E. B. Linscott, *et al.*, Role of spin in the calculation of Hubbard U and Hund's J parameters from first principles, *Phys. Rev. B*, 2018, **98**, 235157, DOI: 10.1103/PhysRevB.98.235157.

25 P. Giannozzi, *et al.*, QUANTUM ESPRESSO: A modular and open-source software project for quantum simulations of materials, *J. Phys.: Condens. Matter*, 2009, **21**, 395502, DOI: 10.1088/0953-8984/21/39/395502.

26 P. Giannozzi, *et al.*, Advanced capabilities for materials modelling with Quantum ESPRESSO, *J. Phys.: Condens. Matter*, 2017, **29**, 465901, DOI: 10.1088/1361-648X/aa8f79.

27 J. P. Perdew, K. Burke and M. Ernzerhof, Generalized gradient approximation made simple, *Phys. Rev. Lett.*, 1996, **77**, 3865–3868, DOI: 10.1103/PhysRevLett.77.3865.

28 S. Grimme, J. Antony, S. Ehrlich and H. Krieg, A consistent and accurate ab initio parametrization of DFT-D for the 94 elements H–Pu, *J. Chem. Phys.*, 2010, **132**, 154104, DOI: 10.1063/1.3382344.

29 B. G. Pfrommer, M. Côté, S. G. Louie and M. L. Cohen, Relaxation of crystals with the quasi-Newton method, *J. Comput. Phys.*, 1997, **131**, 233–240, DOI: 10.1006/jcph.1996.5612.

30 N. Marzari, D. Vanderbilt, A. De Vita and M. C. Payne, Thermal contraction and disordering of the Al(110) surface, *Phys. Rev. Lett.*, 1999, **82**, 3296–3299, DOI: 10.1103/PhysRevLett.82.3296.

31 S. L. Dudarev, *et al.*, Electron-energy-loss spectra and structural stability of nickel oxide: LSDA + U study, *Phys. Rev. B*, 1998, **57**, 1505–1509, DOI: 10.1103/PhysRevB.57.1505.

32 V. L. Campo Jr and M. Cococcioni, Extended DFT+U + V method with on-site and inter-site interactions, *J. Phys.: Condens. Matter*, 2010, **22**, 055602, DOI: 10.1088/0953-8984/22/5/055602.

33 S. Maintz, V. L. Deringer, A. L. Tchougréeff and R. Dronskowski., LOBSTER: a tool to extract chemical bonding from plane-wave based DFT, *J. Comput. Chem.*, 2016, **37**, 1030–1035, DOI: 10.1002/jcc.24300.

34 A. R. Shelke, *et al.*, Electron spectroscopy study of single-crystal CrTe, *Phys. Rev. B*, 2025, **111**, 085142, DOI: 10.1103/PhysRevB.111.085142.

35 Y. Ishida, *et al.*, X-ray magnetic circular dichroism study of $Zn_{1-x}Cr_xTe$, *Appl. Phys. Express*, 2008, **1**, 041301, DOI: 10.1143/APEX.1.041301.

 This journal is © The Royal Society of Chemistry 2026

36 F. Tran, *et al.*, Hybrid exchange-correlation functionals for strongly correlated electrons, *Phys. Rev. B*, 2006, **74**, 155108, DOI: 10.1103/PhysRevB.74.155108.
37 I. Østrøm, *et al.*, Designing 3d metal oxides: selecting optimal density functionals, *Phys. Chem. Chem. Phys.*, 2022, **24**, 14119–14139, DOI: 10.1039/D2CP01303G.
38 I. Timrov, *et al.*, HP code for Hubbard parameters using DFPT, *Comput. Phys. Commun.*, 2022, **279**, 108455, DOI: 10.1016/j.cpc.2022.108455.
39 J. E. Hirsch, Metallic ferromagnetism without exchange splitting, *Phys. Rev. B*, 1999, **59**, 6256–6265, DOI: 10.1103/PhysRevB.59.6256.
40 D. D. Sarma, *et al.*, Electronic structure of Sr_2FeMoO_6, *Phys. Rev. Lett.*, 2000, **85**, 2549–2552, DOI: 10.1103/PhysRevLett.85.2549.
41 R. Sbiaa and S. N. Piramanayagam, Recent developments in spin-transfer torque MRAM, *Phys. Status Solidi RRL*, 2017, **11**, 1700163, DOI: 10.1002/pssr.201700163.
42 I. M. Miron, *et al.*, Perpendicular switching of a single ferromagnetic layer, *Nature*, 2011, **476**, 189–193, DOI: 10.1038/nature10309.
43 J. Han, *et al.*, Room-temperature spin-orbit torque switching induced by a topological insulator, *Phys. Rev. Lett.*, 2017, **119**, 077702, DOI: 10.1103/PhysRevLett.119.077702.
44 E. Goering, X-ray magnetic circular dichroism sum rule correction, *Philos. Mag.*, 2005, **85**, 2895–2911, DOI: 10.1080/14786430500155221.
45 M. D. Watson, *et al.*, Mn-doped Bi_2Te3 single crystals, *New J. Phys.*, 2013, **15**, 103016, DOI: 10.1088/1367-2630/15/10/103016.
46 O. Šipr, Magnetic dipole term and XMCD analysis, *Springer Proc. Phys.*, 2018, **204**, 387–398, DOI: 10.1007/978-3-319-73811-6_29.
47 G. Ponti *et al.*, High Performance Computing & Simulation (HPCS), *IEEE*, 2014, pp. 1030–1033.
48 N Kushwaha, O Armitage, B Edwards, L Trzaska, J Rigden, P Bencok, D Biswas, T-L Lee, C Sanders, G van der Laan, P Wahl and P. D. C King, From ferromagnetic semiconductor to antiferromagnetic metal in epitaxial Cr_xTe_y monolayers, *npj Quantum Mater.*, 2025, **10**, 50.